MHz-Driven Snubberless Soft-Switching Current-Fed Multiresonant DC–DC Converter

Tomokazu Mishima, *Senior Member, IEEE*, Shiqiang Liu, *Student Member, IEEE*, Ryotaro Taguchi, and Ching-Ming Lai, *Senior Member, IEEE*

***Abstract*—A new multiresonant step-up dc–dc converter is proposed in this article, which is suitable for obtaining a high dc–dc voltage ratio with minimizing the counts of active and passive components. The proposed dc–dc converter features the snubberless zero current soft-switching (ZCS) commutation with megahertz (MHz) high-frequency driving of galliumnitride-high electron mobility transistor-based two-phase class-E inverters by adopting quasi resonance and dual parallel load resonance; multiresonant circuitry. The circuit configuration and operation principle are described together with the theory of switch-mode transitions and steady-state power transfer. A frequency-domain analysis is provided on the basis of the equivalent circuit, and the design guideline of multiresonant tanks is provided in details. The essential performances of the proposed dc–dc converter are demonstrated by experiment of a 1-2 MHz / 120 W prototype; ZCS operations are confirmed over the wide range of load variations (40%–100%) with maximum efficiency 91.3% at 86.5% load, electro magnetic interference noise reduction 29%–79% as compared to hard switching, and the voltage ratio 1.5 times higher than the nonmultiresonant topology, and less than 1% low-current ripple factor in the dc inductor.**

***Index Terms*—Current-fed high-frequency inverter, high step-up dc–dc converter, interleaved, multiresonant converter, snubberless, zero current soft-switching (ZCS).**

I. Introduction

A STEP-UP dc–dc converter is the essential power converter for renewable and sustainable power system, transportation electrifications, and a wide variety of circuit topologies have been proposed during the past decades. In particular, the high step-up ratio is one of the critical performance indexes in the dc–dc converters so that the energy utilization is enhanced while efficient power conversion can attain. Downsizing the converter scale is also a technically popular concern in the latest power electronics application, accordingly high-frequency switching, e.g., Megahertz (MHz) driving technique has great relevance with achievement of high power density [1], [2], [3], [4], [5], [6], [7]. The MHz-driven step-up dc–dc converter offers compact and low-profile scale as well as high modularity, the suitable applications of which includes the emerging power electronics applications, such as piezoelectric energy harvester, fuel cell, and class-E power amplifier of wireless power transfer (WPT) [8].

The existing high step-up dc–dc converters are divided into: the stacked connection [9], [10], switched capacitor/inductor [11], [12], [13], voltage multiplier [14], reconfigurable [15], [16], edge resonant [17], [18], and multiresonance [19]. The overview of those existing topologies are summarized in Table I. Those step-up dc–dc converters exhibit high voltage ratio, however, the counts of active and passive components inevitably increase and cost effectiveness may be lost. In contrast, current-fed dc–dc converters with high-frequency link naturally attain voltage step-up by overlapping the ON-duty cycles of two active switches (over 50%). In particular, the two-phase single-ended current-fed dc–dc converter is a good candidate for MHz-driven step-up dc–dc converters in terms of relatively simple circuit topology as well as the common ground gate drivers [20].

The high efficiency and low electromagnetic interference (EMI) noises switching performance plays a key role in the MHz-driven power converters while the related technologies include the developments of materials for magnetic components, such as high-frequency transformer (HF-X) and inductors, and PCB layouts with the reduced leakage inductances [3], [21], [22]. As a soft switching technique for MOS-gated controlled active power devices, zero voltage soft-switching (ZVS) is suitable for treating the capacitive charges in the parasitic capacitances. However, the circulating current inherently is induced in the resonant networks, which leads to the complicated commutation process between the power devices with the aid of auxiliary circuit for the wide range of ZVS performance. In particular, the current-fed dc–dc converter as aforementioned cannot achieve the soft switching without any auxiliary active clamp circuit or active snubber [11]. The quasi-resonant ZVS current-fed dc-dc converters utilizing the leakage inductance of HF-X and the parasitic capacitances of power devices was also proposed in [18]. However, circulating current still exists in the high-frequency inverter stage, thus MHz switching cannot be ensured in the type of current-fed dc–dc converter.

As a solution for the technical limitation and constraint of ZVS, a current-fed dc–dc converter featuring snubberless

Manuscript received 22 September 2023; revised 7 January 2024 and 29 February 2024; accepted 8 March 2024. Date of publication 21 March 2024; date of current version 16 May 2024. Recommended for publication by Associate Editor Y. Yan. *(Corresponding author: Tomokazu Mishima.)*

Tomokazu Mishima, Shiqiang Liu, and Ryotaro Taguchi are with the Division of Marine Technologies and Engineering, Faculty of Oceanology, Kobe University, Hyogo 657-8501, Japan (e-mail: mishima@maritime.kobe-u.ac.jp; 218w903w@stu.kobe-u.ac.jp; 2067059w@stu.kobe-u.ac.jp).

Ching-Ming Lai is with the Division of Electric Engineering, Faculty of Engineering, National Chung Hsing University, Taichung 402, Taiwan (e-mail: pecmlai@dragon.nchu.edu.tw).

Color versions of one or more figures in this article are available at https://doi.org/10.1109/TPEL.2024.3380069.

Digital Object Identifier 10.1109/TPEL.2024.3380069

TABLE I
COMPARISON OF HIGH STEP-UP DC–DC CONVERTERS

Circuit topology	References	Numbers of power devices/ passive comp.	Switching frequency/ Pulse modulation	Input/output Voltages	Soft-switching Efficiency
stacked connection	[9]	4/6	50 kHz/PWM	20 V/400 V	NR 94/1 %@320 W
	[10]	7/5	50 kHz/PWM	20 V/402 V	NR 93.3 %@250 W
switched capacitor/inductor	[12]	6/6	100 kHz/PWM	30–40 V/600 V	ZVS 97.0 %@600 W
	[13]	9/8	40 kHz/PWM	30 V/400 V	NR 94 %@200 W
voltage multiplier and stack	[15]	6/6	50 kHz/PWM	5–10 V/50–100 V	NR 94 %@400 W
reconfigurable	[16]	8 ≤	62-54 kHz PFM	24–54 V/800 V	ZVS 96.1 %@600 W
edge resonance	[18]	4/6	50 kHz/PWM	45 V/380 V	ZVS 95.7 %@400 W
multi-resonance	[19]	4N/ 1+2N (N-stage)	20 MHz/ON&OFF	15.7–30 V/60 V	ZVS/ZCS ≤ 96.5 %@200 W
snubberless	[23]	2/2	1-2 MHz PFM	10 V/85 V	ZCS 86.1 %@70 W

*Counted by a discrete power device. NR: not reported.

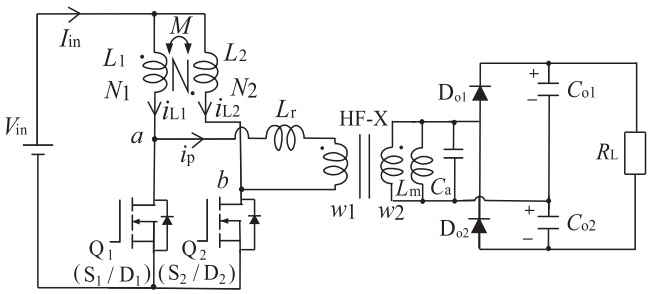

Fig. 1. Snubberless ZCS step-up DC–DC converter [23].

zero current soft-switching (ZCS) of GaN-HEMT with MHz switching was proposed as schematically drawn in Fig. 1 [23]. This topology is based on the quasi-resonant and LC resonant converters, and is free from the parasitic ringings of active switches which is inherent to the ZCS-pulsewidth modulation (PWM) dc–dc converters [24], owing to the voltage-clamping effect on the parallel capacitor in the secondary-side of HF-X. Although the similar approach was proposed in the past decade [25], the originality exists in the MHz driving by snubberless structure together with the dc coupled inductors for further reduction of passive components. The technical constraint of the previously proposed topology in [23] is the voltage ratio inherently depends on the transformer turns ratio and voltage doubler rectifier. Thus, the technical challenge of the snubberless dc–dc converter is how to enhance the step-up ratio by decoupling the edge resonance and parallel load resonance.

In order to overcome the technical constraint on increasing the step-up ratio, a new multiresonant high step-up dc–dc converter is proposed in this article. The multiresonant circuitry in the secondary-side of HF-X is dedicated for lifting the voltage without losing the merits of snubberless structure. Therefore, snubberless ZCS technique with multiresonant tank is attractive for the MHz-driven current-fed dc–dc converter in terms of soft switching range, counts of active and passive components, as well as reduction of reactive current. The novelty and originality exist in the multiresonant topology; edge-resonant for ZCS, antiresonant for reduction of magnetizing current in the HF-X, and parallel-load resonant for high step-up ratio, all of which are comprised by only the passive components under the conditions of MHz switching. It is suitable and beneficial for MHz-driven power converter in terms of practical and cost-effective circuit topology since no additional active switches are necessary together with the snubber components. In addition, the simplicity, high step-up voltage ratio, low current ripple in the dc input source together with the galvanic isolation are significantly advantageous for renewable power generation systems and energy harvest devices, such as photovoltaic, liquid hydrogen/fuel cells and piezoelectric devices applied for the industry, distributed power, automotive, home, and consumer electronics.

The article [23] was dedicated for the basic and original type of MHz-driven snubberless ZCS dc–dc converter, where the operation principle and analysis on the PFM-based power regulations were described and followed by the experimental verification on the snubberless topology. It leads to the original idea of high step-up dc–dc converter with simple but practical circuit topology as treated herein. It is true that the newly proposed dc–dc converter is modified and extended from the basic type by adding the parallel load resonant tank in the secondary side. However, the strategies on analysis and design of the main circuit have the different approaches from the basic type in terms of resonant converters, accordingly the descriptions and experimental results are different from [23].

The rest of this article is organized as follows: The circuit topology and operation principle of the proposed multiresonant dc–dc converter are described in Section II. The steady-state characteristics of dc–dc voltage ratio are revealed in the frequency-domain analysis, whereby the pulse-frequency-modulation (PFM)-based load voltage and power regulations are theoretically explained in Section III. In addition, the design

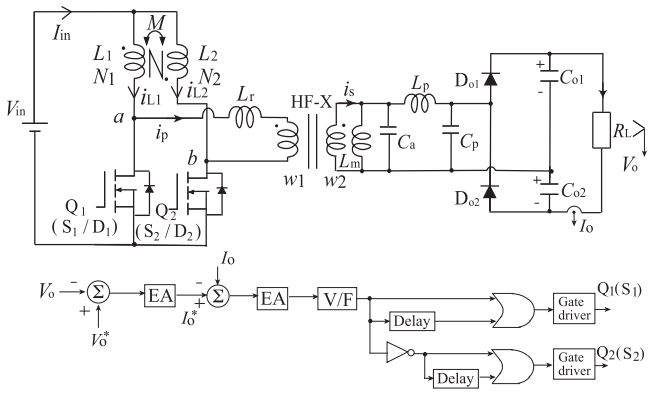

Fig. 2. Proposed multiresonant high step-up DC–DC converter with power controller.

guideline of circuit parameters is also presented in the same section so that the snubberless ZCS and high step-up voltage regulation attain simultaneously. The switching performances and steady-state characteristics on the load power and voltage ratio are investigated together with electromagnetic noises by experiment in Section IV, after which the effectiveness of the proposed dc–dc converter is verified from the practical point of view in Section V.

II. Circuit Topology and Operation Principle

The circuit topology of the proposed high step-up dc–dc converter is described with PFM-based power controller in Fig. 2.

The power stage of the primary-side HF-X consists of the current-fed two-phase class-E inverters which operate by the interleaved gate clocking in the active switches Q_1 and Q_2. Note here that any additional capacitive snubbers are not necessary in the two-phase class-E inverters. The secondary-side HF rectifier comprises of an antiparallel capacitor C_a and the parallel-load resonant circuit L_p-C_p, the latter of which works for voltage lifting. The secondary-side rectifier of HF-X is the voltage doubler, and other multiplier rectifiers can be candidates in accordance with the step-up ratio. The controller consists of voltage and current dual loops of the dc load. The pulse modulations is based on PFM and over 50% ON-duty ratio in Q_1 and Q_2. The load voltage is detected and compared with its reference, after which their difference is processed by error amplifier (EA). The output of the voltage EA is the command value to the load current, and the current loop with the another EA generates the control value. The control signal is processed by V/F converter, and ON-duty signal is generated by V/F converter. The pulse signal from the V/F converter is feed to a time delay circuit corresponding to the edge-resonant interval, then the gate signal of S_1 is produced through an OR logic circuit. The counterpart of gate signal S_2 is also generated by the same logic with 180° of phase shift by a NOT gate.

The key operating waveforms of the main circuit and gate signals are depicted in Fig. 3. The ZCS commutations complete at the intervals of the two-switch overlapping "ON" states. The dc current ripples in i_{L1} and i_{L2} are ideally canceled out by

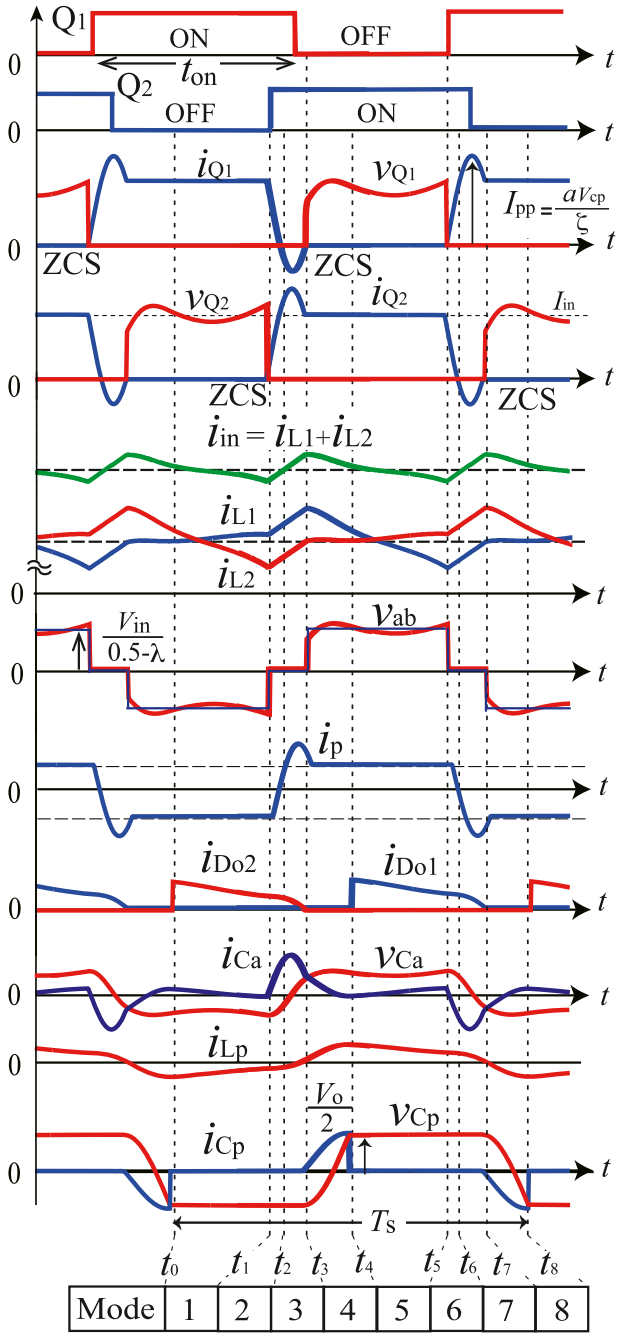

Fig. 3. Key voltage and current waveforms during the switching one cycle.

the interleaved manner, so that the low ripple in the input side can maintain as low profile. The voltage v_{Ca} across C_a is lifted by the effect of the antiparallel load resonant tank L_p-C_p.

The mode transitions of switching one-cycle can be divided into eight modes, as depicted in Fig. 4. The ideal conditions are given as follows: 1) The inductance of L_1 and L_2 are identical as expressed by $L_d = L_1 = L_2$; 2) the on-resistances of Q_1 and Q_2 are small enough to neglect. The dc inductor currents i_{L1}, i_{L2} can be expressed in each mode while the steady-state time-domain equations of the other variables are summarized in the Appendix.

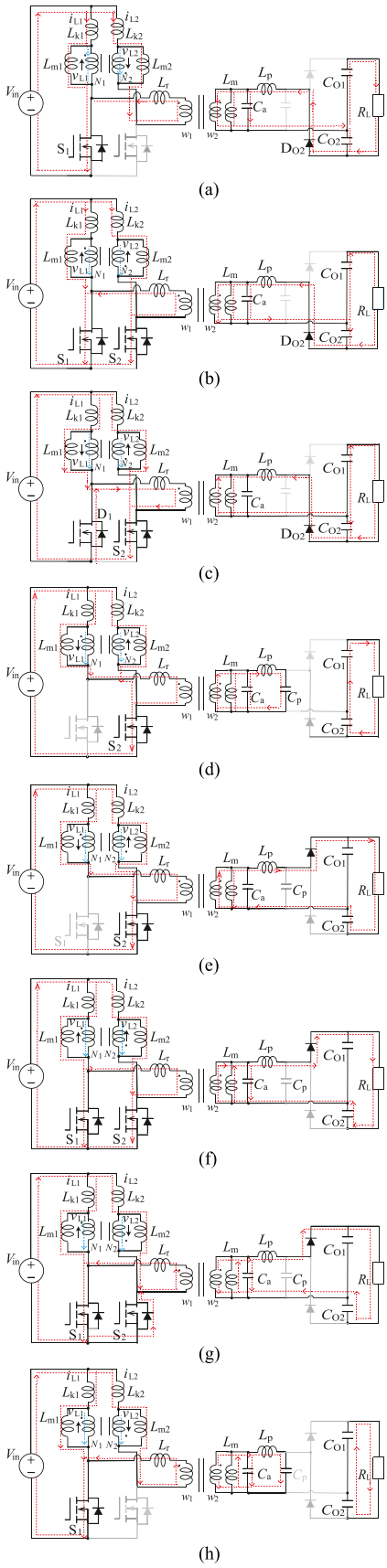

Fig. 4. Mode transitions and equivalent circuits during the switching one cycle. (a) Mode 1. (b) Mode 2. (c) Mode 3. (d) Mode 4. (e) Mode 5. (f) Mode 6. (g) Mode 7. (h) Mode 8.

[Mode 1 ($t_0 \le t < t_1$). Power transfer mode]: The active switch S_1 keeps ON-state while Q_2 is OFF in this interval. Then, the magnetic energy is stored in L_1 while it is released to the load. The dc inductor currents can be expressed by

$$i_{L1}(t) = \frac{(1+k)V_{in} - kav_{ca}}{(1-k^2)L_d} \cdot (t - t_0) + i_{L1}(t_0) \quad (1)$$

$$i_{L2}(t) = \frac{(1+k)V_{in} - av_{ca}}{(1-k^2)L_d} \cdot (t - t_0) + i_{L2}(t_0) \quad (2)$$

where k is the coupling coefficient of the coupled dc inductors L_1, L_2 while a $(= w_1/w_2)$ denotes the windings turns ratio of the HF-X.

[Mode 2 ($t_1 \le t < t_2$). Edge resonant mode (Q_2 ZCS turn-on)]: The active switch S_2 is turned ON at t_1, then the edge resonance begins by the leakage inductance L_r and the parallel capacitor C_a in the secondary-side power stage. The polarity of the HF-X primary windings current i_p naturally changes, and the capacitor voltage v_{ca} increases gradually with the aid of L_r-C_p edge resonance. The dc inductor currents are expressed by

$$i_{L1}(t) = \frac{(1+k)V_{in}}{(1-k^2)L_d} \cdot (t - t_1) + i_{L1}(t_1) \quad (3)$$

$$i_{L2}(t) = \frac{(1+k)V_{in}}{(1-k^2)L_d} \cdot (t - t_1) + i_{L2}(t_1). \quad (4)$$

The primary-side transformer winding current i_p is expressed by

$$i_p(t) = \frac{av_{ca}}{\zeta} \sin\{\omega_q(t - t_1)\} + i_p(t_1) \quad (5)$$

$$i_p(t_1) = \frac{i_s(t_1)}{a} \simeq 2I_o \quad (6)$$

$$\zeta = a\sqrt{\frac{L_r}{C_a}}, \quad \omega_q = \frac{a}{2\pi\sqrt{L_r C_a}}. \quad (7)$$

[Mode 3 ($t_2 \le t < t_3$). Edge-resonant mode (Q_1 ZCS turn-OFF)]: The switch current i_{Q_1} naturally reaches to zero at t_2. By removing the gate-signal during this interval, ZCS turn-OFF can attain in Q_1. The condition of ZCS commutation from Q_2 to Q_1 is defined as

$$\zeta < \frac{v_{\mathrm{ca}}}{2I_o}. \quad (8)$$

[Mode 4 ($t_3 \le t < t_4$). Parallel-load resonant mode]: The switch current i_{Q2} is identical to the dc input current i_{in} at $t = t_3$, whereby the edge resonance is terminated. The switch current i_{L2} increases linearly while S_2 keeps ON-state

$$i_{L1}(t) = \frac{(1+k)V_{in} - av_{\mathrm{ca}}}{(1-k^2)L_d} \cdot (t - t_3) + i_{L1}(t_3) \quad (9)$$

$$i_{L2}(t) = \frac{(1+k)V_{in} - kav_{\mathrm{ca}}}{(1-k^2)L_d} \cdot (t - t_3) + i_{L2}(t_3). \quad (10)$$

[Mode 5 ($t_4 \le t < t_5$). Power transfer mode]: The voltage v_{Cp} across the parallel load-resonant capacitor C_p exceeds to the voltage $V_{C_{o1}}$ at $t = t_4$, and the rectifying diode D_{o1} is forward-biased.

[Mode 6 ($t_5 \le t < t_6$). Edge-resonant mode (Q_1 ZCS turn-ON)]: The switch S_1 is turned ON at $t = t_5$, then the edge

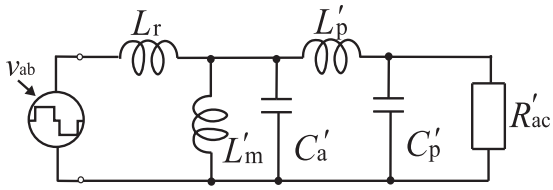

Fig. 5. Simplified equivalent circuit with the primary-side referred parameters: $L'_m = a^2 L_m$, $L'_p = a^2 L_p$, $C'_a = C_a/a^2$, $C'_p = C_p/a^2$, and $R'_{ac} = a^2 R_{ac}$.

resonance is resumed. The current i_{Q1} increases gradually, and ZCS turn-ON can attain in Q_1. The dc inductor currents are expressed by

$$i_{L1}(t) = \frac{(1+k)V_{in}}{(1-k^2)L_d} \cdot (t - t_5) + i_{L1}(t_5) \tag{11}$$

$$i_{L2}(t) = \frac{(1+k)V_{in}}{(1-k^2)L_d} \cdot (t - t_5) + i_{L2}(t_5) \tag{12}$$

$$i_p(t) = \frac{av_{ca}}{\zeta} \sin\{\omega_r(t - t_5)\} + i_p(t_5) \tag{13}$$

$$i_p(t_5) = \frac{i_s(t_5)}{a} \simeq 2I_o. \tag{14}$$

[Mode 7 ($t_6 \le t < t_7$). Edge-resonant mode (Q_2 ZCS turn-OFF)]: The switch current i_{Q_2} naturally reverses its direction at $t = t_6$, then the diode D_2 of Q_2 is conducting. During this interval, the gate signal to S_2 is removed, then ZCS turn-OFF can attain in Q_2.

[Mode 8 ($t_7 \le t < t_8$). Parallel-load resonant]: The switch current i_{Q_1} is equal to the input current i_{in} at $t = t_7$, whereby the edge resonance is terminated. The two dc inductor currents i_{L_1} and i_{L_2} flows into Q_1; i_{L_1} linearly increases while i_{L_2} gradually decreases

$$i_{L1}(t) = \frac{(1+k)V_{\text{in}} - \text{kav}_{\text{ca}}}{(1-k^2)L_d} \cdot (t - t_7) + i_{L1}(t_7) \tag{15}$$

$$i_{L2}(t) = \frac{(1+k)V_{\text{in}} - av_{\text{ca}}}{(1-k^2)L_d} \cdot (t - t_7) + i_{L2}(t_7). \tag{16}$$

III. Steady-State Characteristics

A. Frequency-Domain Analysis

The simplified equivalent circuit is depicted in Fig. 5. Assuming that the power losses in C_{o1} and C_{o2} are small enough for neglecting, the sinusoidal approximation theory can be applied for the proposed topology. Thus, the ac equivalent resistance R_{ac} can be expressed by

$$R_{ac} = \frac{2V_o}{\pi^2 I_o} = \frac{2}{\pi^2} R_L. \tag{17}$$

The impedance Z_{in} viewed from the input dc source V_{in} can be defined as [26]

$$\dot{Z}_{\text{in}} = \dot{Z}_{i0} \frac{1 + \frac{R'_{ac}}{\dot{Z}_{o0}}}{1 + \frac{R'_{ac}}{\dot{Z}_{o\infty}}} = \dot{Z}_{i\infty} \frac{1 + \frac{\dot{Z}_{o0}}{R'_{ac}}}{1 + \frac{\dot{Z}_{o\infty}}{R'_{ac}}} \tag{18}$$

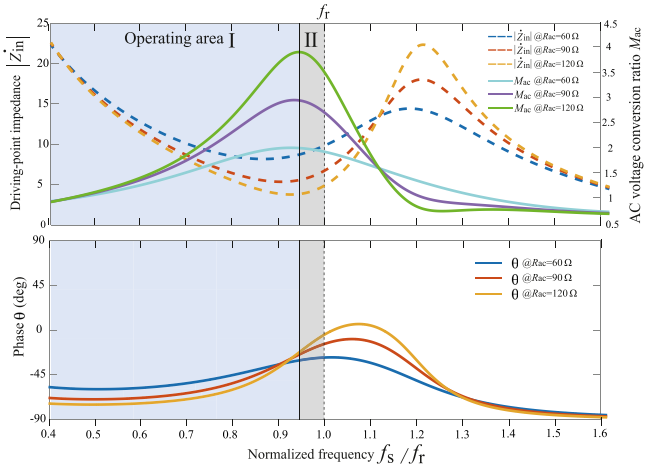

Fig. 6. Frequency-domain characteristics of the driving-point impedance ($\dot{Z}_{in}$) in the AC equivalent circuit ($L_r = 44\,\text{nH}$, $L_m = 25.6\,\mu\text{H}$, $C_a = 2.2\,\text{nF}$, $L_p = 2\,\mu\text{H}$, $C_p = 1\,\text{nF}$, and $a = w_1/w_2 = 1/2$).

where each impedance can be expressed as

$$\dot{Z}_{i0} = \frac{1}{j\omega C'_a + \frac{L'_m + L'_p}{j\omega L'_m L'_p}} + j\omega L_r \tag{19}$$

$$\dot{Z}_{i\infty} = \dot{Z}_1 + j\omega L_r$$

$$\dot{Z}_1 = \left\{ j\omega C'_a + \frac{1}{j\omega L'_m} + \frac{1}{j\omega L'_p + \frac{1}{j\omega C'_p}} \right\}^{-1} \tag{20}$$

$$\dot{Z}_{o0} = \frac{1}{j\omega C'_p + \dot{Z}_3^{-1}}, \; \dot{Z}_3 = j\omega L'_p + \dot{Z}_2 \tag{21}$$

$$\dot{Z}_2 = \left\{ \frac{L'_m + L_r}{j\omega L'_m L_r + j\omega C'_a} \right\}^{-1} \tag{22}$$

$$\dot{Z}_{o\infty} = \frac{1}{\frac{1}{\dot{Z}_4 + j\omega L'_p} + j\omega C'_p}$$

$$\dot{Z}_4 = \left\{ j\omega C'_a + \frac{1}{j\omega L'_m} \right\}^{-1}. \tag{23}$$

Accordingly, the ac voltage ratio M_{ac} can be expressed as

$$M_{ac} = \left| \left(1 - \frac{j\omega L_r}{\dot{Z}_{\text{in}}} \right) \cdot \left(\frac{1}{j\omega L'_p \dot{Y}_5 + 1} \right) \right| \tag{24}$$

$$\dot{Y}_5 = j\omega C'_p + R'^{-1}_{\text{ac}}. \tag{25}$$

The frequency characteristics of Z_{in} and M_{ac} are drawn in Fig. 6 by referring to (18) and (24) with a set of numerical example. The operating area should be set as the capacitive load area where the switching frequency is less than the resonant frequency of maximum ac voltage gain in M_{ac}.

On the other hand, the dc voltage ratio $G\,(= V_o/V_{in})$ should be derived from the viewpoint of power balance between the input and output in Fig. 5. In order to simply the analysis on the high-order resonant tank, the two-phase class-E inverter voltage v_{ab} is

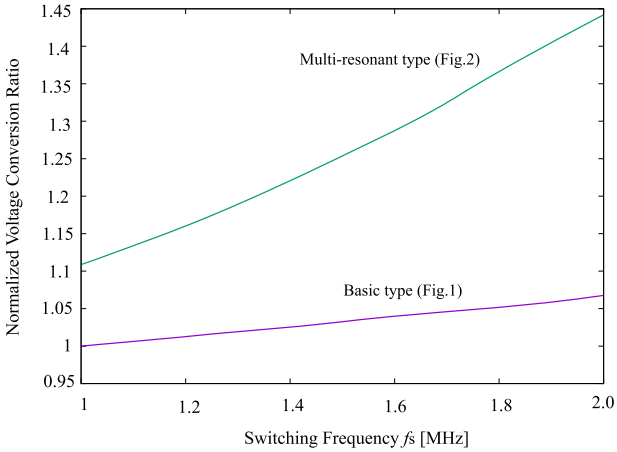

Fig. 7. Theoretical characteristics of the DC–DC voltage conversion ratios (normalized by the voltage ratio of the basic type at 1 MHz).

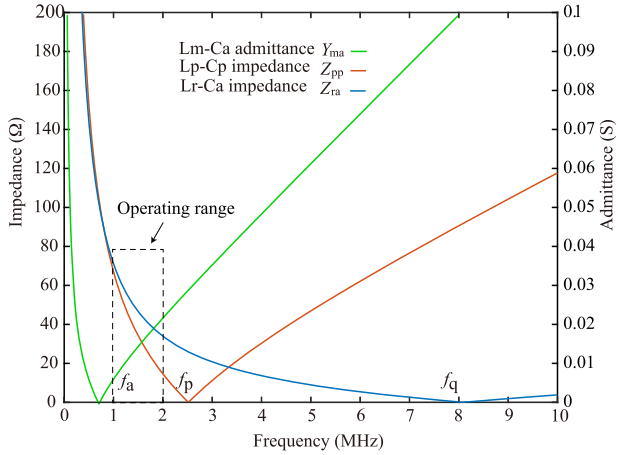

Fig. 8. Impedances of the edge-resonant L_r-C_a, the load-resonant L_p-C_p, and admittance of the antiresonant tank L_m-C_a ($L_r = 44\,\text{nH}$, $L_m = 25.6\,\mu\text{H}$, $C_\text{a} = 2.2\,\text{nF}$, $L_p = 2\,\mu\text{H}$, $C_p = 1\,\text{nF}$, and $a = w_1/w_2 = 1/2$).

linearly expressed in Fig. 2. Note here that linearization follows to the method in [23].

The dc voltage ratio of G both for the basic and multiresonant types can be defined by

$$G = \frac{\sqrt{2}\,aR_L}{\pi} \times \frac{2\sqrt{2}V_{in}}{\pi\,(0.5-\lambda)} \sqrt{\sum\nolimits_{n=1,3,5..}^{\infty} \frac{\cos^2(\lambda n\pi)}{n^2 z_n^2}} = \frac{4aR_L}{\pi^2\,(0.5-\lambda)} \sqrt{\sum\nolimits_{n=1,3,5..}^{\infty} \frac{\cos^2(\lambda n\pi)}{n^2 z_n^2}} \tag{26}$$

where λ is defined as

$$\lambda = \frac{4\pi\sqrt{L_r C_a}\cdot f_s}{5a}. \tag{27}$$

In addition, Z_n in (26) denotes $Z_{n,b}$ in (28) for the basic type and $Z_{n,\text{mr}}$ in (29) shown at the bottom of this page for the multiresonant type, respectively,

$$Z_{n,b} = \sqrt{R_{\text{ac}}^2 \left(a^2 + \frac{L_r}{L_m} - n^2\omega^2 L_r C_a\right)^2 + n^2\omega^2 L_r^2} \tag{28}$$

The dc–dc voltage ratios of the proposed topologies are compared in Fig. 7 between the basic and proposed topologies. It can be known from the comparison that higher voltage ratio can achieve in the proposed converter.

B. Design of Parameters in Resonant Tank

The impedances Z_{ra}, Z_{pp} of the edge resonant L_r-C_a and parallel-load resonant L_p-C_p, and admittance Y_{ma} of antiresonant L_m-C_a are presented in Fig. 8. The resonant frequencies can be defined as

$$f_a = \frac{1}{2\pi\sqrt{L_m C_a}},\ f_p = \frac{1}{2\pi\sqrt{L_p C_p}},\ f_q = \frac{a}{2\pi\sqrt{L_r C_a}} \tag{30}$$

where the condition expressed by $f_a < f_s < f_p < f_q$ should be satisfied. Once the ratios between the two frequencies are defined as

$$\alpha = \frac{f_p}{f_a},\quad \beta = \frac{f_q}{f_p} \tag{31}$$

where the relationships between magnetizing L_m, the parallel capacitor C_a, and leakage inductance L_r are expressed by

$$C_a = \frac{1}{{\omega_a}^2 L_m},\quad \omega_a = 2\pi f_a \tag{32}$$

$$L_r = \frac{1}{{\omega_q}^2 C_a},\quad \omega_q = 2\pi f_q. \tag{33}$$

It can be understood from Fig. 6 that the frequency range between f_a and f_q is most suitable for obtaining the effects of anti and parallel-load resonant while edge-resonant frequency should exist in the higher frequency area. Accordingly, the antiresonant frequency f_a should be set in the area smaller than 1 MHz for deciding the switching frequency between 1 and

$$Z_{n,\text{mr}} = \frac{L_m}{L_r}\cdot\sqrt{\alpha^2+\beta^2}$$

$$\alpha = R_{\text{ac}}\left\{1 + \frac{a^2 L_m}{L_r} + \left(\frac{n\omega}{\omega_a}\cdot\frac{n\omega}{\omega_p}\right)^2 - \left(\frac{n\omega}{\omega_a}\right)^2 - \left\{1 + \frac{L_m(L_r + a^2 L_p)}{L_r L_p}\right\}\left(\frac{n\omega}{\omega_p}\right)^2\right\}$$

$$\beta = n\omega L_p\left\{1 + \frac{L_m(L_r + a^2 L_p)}{L_r L_p} - \left(\frac{n\omega}{\omega_a}\right)^2\right\}. \tag{29}$$

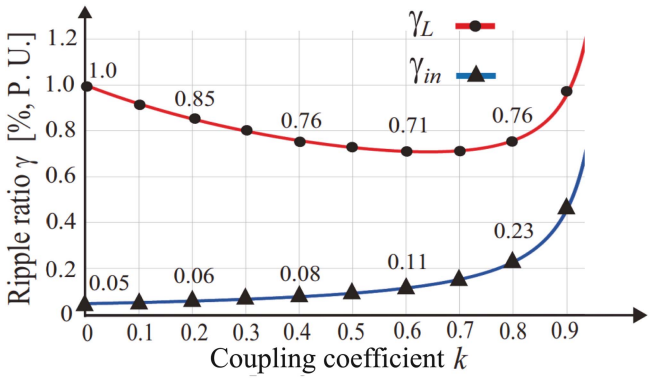

Fig. 9. Current ripple ratios versus magnetically coupling coefficient in the DC side.

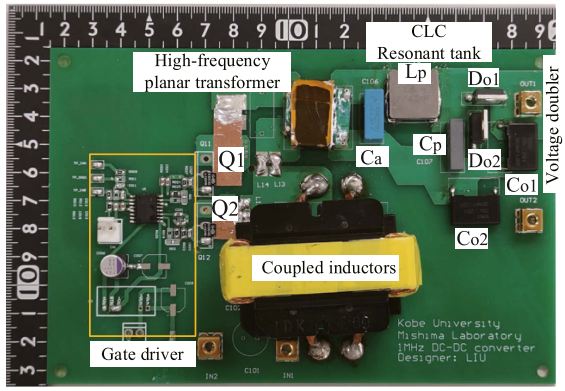

Fig. 10. Exterior appearances of prototype.

2 MHz; Y_{ma}, $Z_{pp} < Z_{ra}$. Thus, α and β should be greater than 1, respectively. By adjusting α and β until the ZCS condition (8) is satisfied, the parameters of C_a and L_r can be determined by (32) and (33). Thereby, α and β ($\alpha < \beta$) are decided between 1 and 3 from the practical point of views for MHz driving.

Furthermore, when the quality factor Q in the parallel load resonant tank is set as the practical value, e.g., $1 < Q < 10$, L_p can be decided by

$$L_p = \frac{R_{ac}}{\omega_p Q}, \quad \omega_p = 2\pi f_p. \tag{34}$$

Thus, the capacitor C_p can be obtained as

$$C_p = \frac{1}{{\omega_p}^2 L_p}. \tag{35}$$

C. Coupled DC Inductors

The ripple factors of the two dc inductors can be defined by referring to one of the modes where they gradually increase. Now, by giving the average inductors currents I_L, I_{in}, respectively, the ripple factors can be defined as

$$\gamma_L = \frac{(1+k)V_{in} - av_{ca}}{(1-k^2)L_d I_L f_s}(1-D) \tag{36}$$

$$\gamma_{in} = \frac{2V_{in} - av_{ca}}{(1-k)L_d I_{in} f_s}(1-D) \tag{37}$$

where D ($= t_{on}/T_s$) is the ON-duty cycle of Q_1 and Q_2. The curves of current ripples are illustrated in Fig. 9 according to (36) and (37) with a set of numerical examples ($V_{in} = 10$ V, $L_d = L_1 = L_2 = 25\,\mu$H, $v_{ca} = 2V_{in}$). It can be known that γ_L is minimum at $k = 0.6$ while γ_{in} increases gradually in accordance with the increase of k.

IV. Experimental Evaluations

A. Specification of Prototype

The performances of proposed dc–dc converter are evaluated by experiment of 1–2 MHz / 120 W prototype with GaN-HEMT (GS61004B, $V_{DS} = 100$ V, $I_{DS} = 38$ A, $R_{DS,on} = 16\,m\Omega$, $C_{oss} = 110$ pF, $Q_g = 3.3$ nC, GaN Systems) for Q_1, Q_2, and Silicon Carbide Schottky diode (SiC-SBD) (IDH06G65C6, 650 V, 6 A, typical V_F: 1.25 V, Infenion) for D_{o1}, D_{o2}, respectively. The exterior appearance of prototype is portrayed in Fig. 10. The circuit parameters and specification are displayed in Table II. Selection of 1.8 MHz for the rated power can be justified in line with the technical trend of automotive applications; 1.8–2.2 MHz is preferably selected in order to mitigate EMI from the dc–dc power converters.

TABLE II
Circuit Parameters of Prototype

Item	Symbol	Value
DC input voltage	V_{in}	10 V
DC output voltage	V_o	85-160 V
Output power rating	P_o	120 W
Nominal Switching frequency	f_s	1.8 MHz
Anti-resonant frequency	f_a	680 kHz
Load resonant frequency	f_p	3.8 MHz
Edge-resonant frequency	f_q	8.1 MHz
Duty cycle	D	0.56
Input dc inductor	L_1	71 μH
Input dc inductor	L_2	73 μH
L_1, L_2 windings turns ratio	$n(= N_1/N_2)$	1
Mutual inductance	M	43 μH
Coupling coefficient	k	0.59
HF-X magnetizing inductance	L_m	26 μH
HF-X leakage inductance	L_r	45 nH
HF-X windings turns ratio	$a(= w_1/w_2)$	1/2
Antiresonant capacitor	C_a	2.2 nF
Load-resonant capacitor	C_p	1 nF
Load-resonant inductor	L_p	1.8 μH
Voltage dividing capacitors	$C_{o1,2}$	180 nF

The planar transformer is designed for 1–2 MHz switching, and its core material is MnZn ferrite (PC200, ER-23/5/13). The magnetic core selection is based on a maximum magnetic flux density. The gate resistors of Q_1 and Q_2 are decided as 10 Ω for minimizing parasitic ringings in MHz driving. The quality factor Q of L_p-C_p resonant tank in (34) is given as 2 at the nominal $R_L = 200\,\Omega$.

B. Switching Performances and Steady-State Characteristics

The switching waveforms of the prototype can be observed in Fig. 11 for $f_s = 1.1$ MHz (light load) and 1.5 MHz (heavy

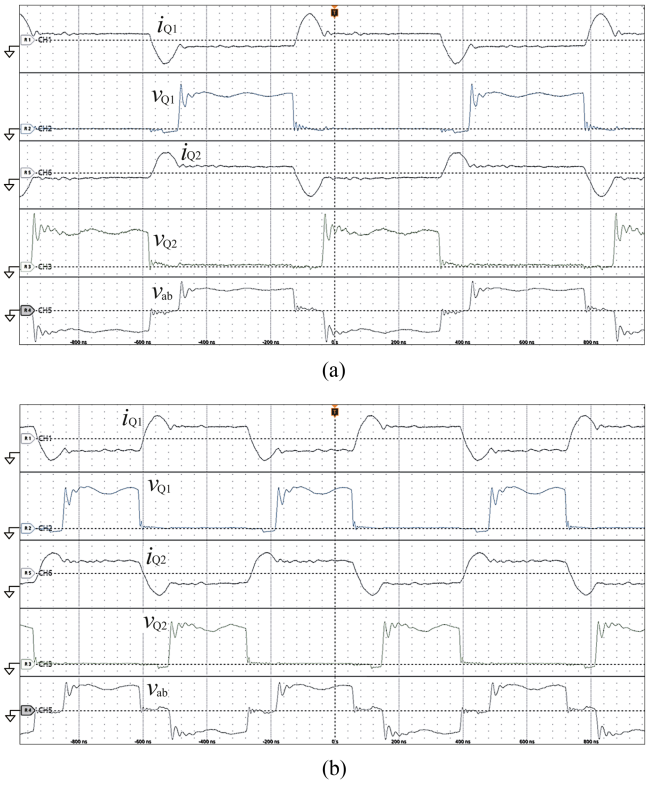

Fig. 11. Observed switching waveforms of active switches at: (a) $f_s = 1.1\,\mathrm{MHz}$ and $P_o = 51\,\mathrm{W}$ (i_{Q1}, i_{Q2}:2.5 A/div, v_{Q1}, v_{Q2}:6 V/div, v_{ab}:10 V / div, 200 μs/div), and (b) $f_s = 1.5\,\mathrm{MHz}$ and $P_o = 104,\mathrm{W}$ (i_{Q1}, i_{Q2}:2.5 A/div, v_{Q1}, v_{Q2}:6 V/div, v_{ab}:10 V / div, 200 μs/div).

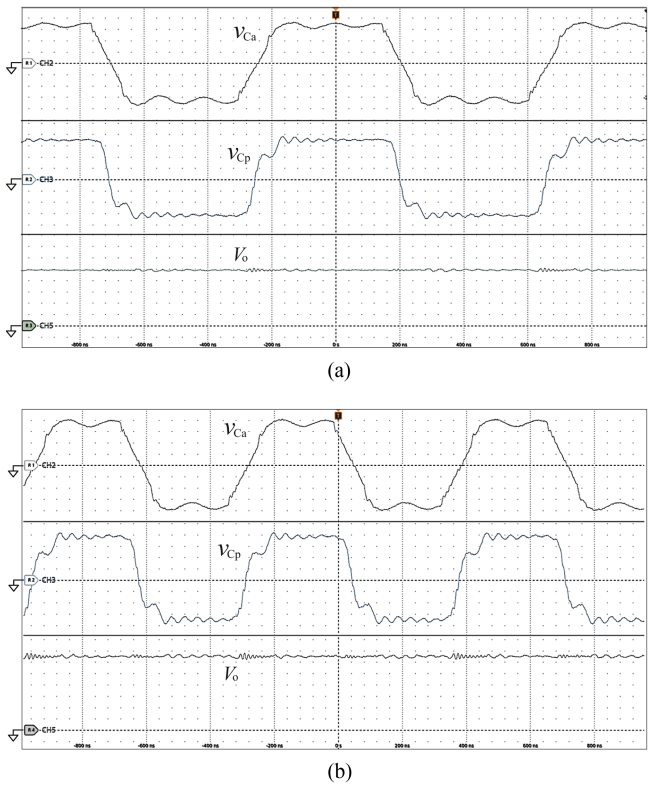

Fig. 12. Observed capacitor waveforms at: (a) $f_s = 1.1\,\mathrm{MHz}$ and (b) $f_s = 1.5\,\mathrm{MHz}$ (v_{Q2}:15 V/div, v_{ab}:15 V / div, V_o:20 V / div, 200 μs/div).

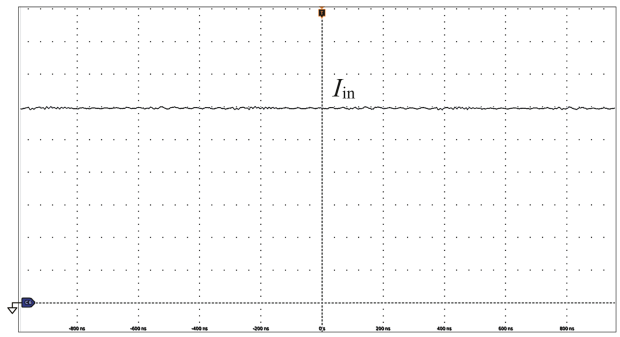

Fig. 13. Observed waveform of the dc input current I_{in} (2 A / div, and 200 μs/ div).

load), respectively. It can be observed in each cases that the current i_{Q_1} gradually declines by edge resonant while the current i_{Q_2} gradually increases, which leads to ZCS turn-ON in Q_2 and ZCS turn-OFF in Q_1, respectively. After the power transfer interval, i_{Q_1} starts to increase with a certain slope from zero by supplying the gate signal to S_1 while i_{Q_2} declines gradually, which leads to ZCS turn-ON in Q_1 and ZCS turn-OFF in Q_2, respectively. Thus, the feasibility of snubberless ZCS topology is verified for the light and heavy load conditions.

The resonant capacitor voltages v_{C_a} and v_{C_p} are also observed in Fig. 12. The amplitude of the parallel-resonant capacitor v_{C_p} are lifted from that of v_{C_a} at both the light and heavy loads, and the double voltage appears in the output voltage V_o with the effect of the voltage doubler rectifier. Thus, step-up operations of the multiresonant tank are demonstrated hereby.

The dc input current I_{in} is shown in Fig. 13. The ripple current is less than 0.1% for the average dc current 12 A: γ_{in} is 0.83% while the theoretical value is calculated as 0.63% at $v_{\mathrm{ca}} = 56\,\mathrm{V}$ from (37). Thus, the effectiveness of (37) is verified herein.

The radiated noise emissions are measured by comparing with hard switching conditions in Fig. 14. The radiated noise is reduced by 29% from 11.4 to 8.1 μW at $f_s = 1.5\,\mathrm{MHz}$ due to the snubberless ZCS. Furthermore, it is reduced by 79% from 134.8 to 27.8 μW at $f_s = 18\,\mathrm{MHz}$. Thus, the effectiveness of snubberless ZCS is proven in the experimental result.

The steady-state characteristics of input–output dc voltage ratio G are measured under the open loop control in Fig. 15. More than 16 of G can attain in the proposed topology, and 1.5 times higher than the previously proposed topology in Fig. 1. The maximum voltage ratio is 16 at $f_s = 2\,\mathrm{MHz}$. Therefore, the higher voltage step-up can be achieved in Fig. 15.

The steady-state characteristics of output power versus switching frequency are measured under the condition of $V_o = 120\,\mathrm{V}$ in Fig. 16. It can be confirmed from the curve that P_o increase gradually from 51 W with $f_s = 1.1\,\mathrm{MHz}$ up to about 120 W at $f_s = 1.8\,\mathrm{MHz}$. The complete ZCS operation can be obtained in the switching frequency 1 to 1.8 MHz. Thus, the effectiveness of PFM-based power regulation with the snubberless ZCS is revealed in the curves.

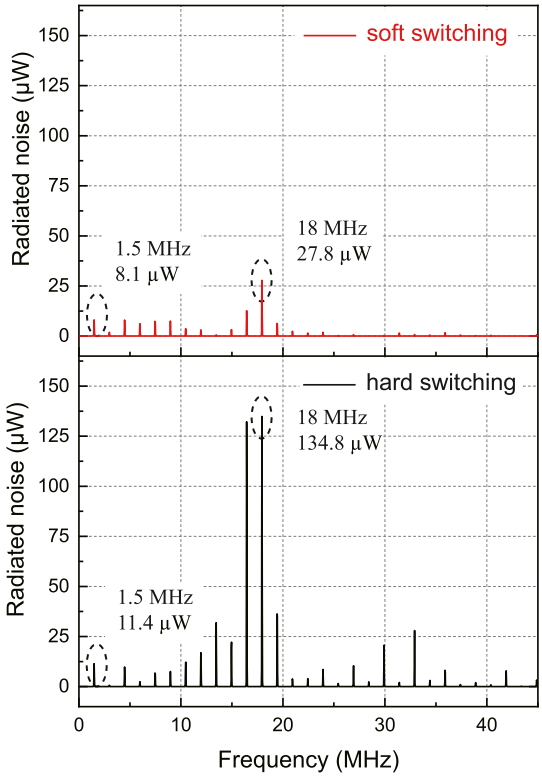

Fig. 14. Observed spectrum of radiated noises (probing by Electro-Metrics EM-6992).

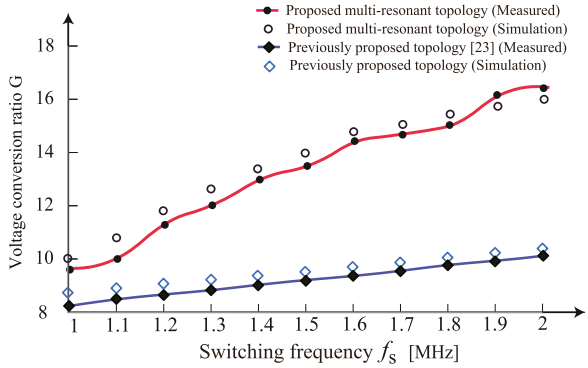

Fig. 15. Comparison of step-up DC–DC voltage ratio (open-loop condition).

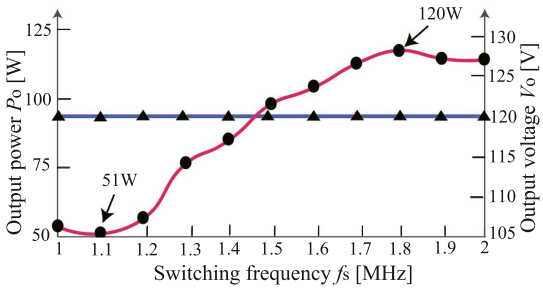

Fig. 16. Output power versus switching frequency curves at $V_o = 120\,\mathrm{V}$.

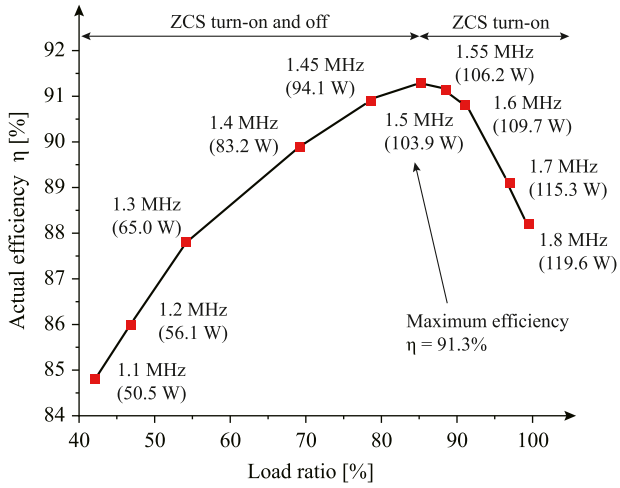

Fig. 17. Actual efficiency curves for load variations.

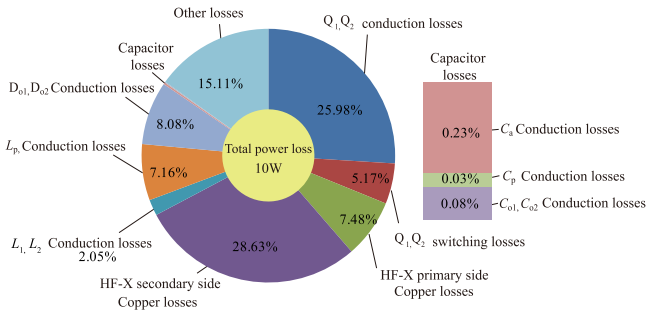

Fig. 18. Power loss breakdown at $f_s = 1.5\,\mathrm{MHz}$, $P_o = 104\,\mathrm{W}$ and $\eta = 91.3\%$.

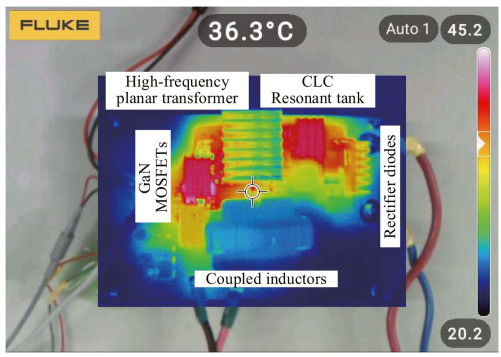

Fig. 19. Thermography image of prototype in ten minutes after the start up at 24.5 °C of the room temperature.

C. Power Conversion Efficiency and Loss Analysis

The actual efficiency of the prototype is presented in Fig. 17. The ZCS turn-ON and -OFF operations can maintain up to 86.5% load ($P_o \simeq 104\,\mathrm{W}$, $f_s = 1.5\,\mathrm{MHz}$) while ZCS turn-OFF cannot attain from 86.5% to 100% load since (8) cannot be satisfied. The maximum efficiency is recorded as 91.3% at 86.5% load, and over 90% efficiency can be ensured in the load ratio of 70%–92%.

TABLE III
COMPARISON OF MHZ-DRIVEN DC–DC CONVERTERS

Circuit topology	Galvanic isolation	Switching frequency	Modulations	Input/output Voltages	Soft-switching Peak Efficiency Power device	Power density
Two-phase half-bridge[27]	isolated	1 MHz	PWM	36 V-60 V/1.8 V (buck)	ZVS&ZVS NR@90 W GaN-HEMT (EPC2014)	-
Current-fed active-clamped[28]	isolated	1 MHz	PWM	25 V/100 V (boost)	ZVS – –	–
DC-X[29]	isolated	1 MHz/300 kHz	PWM	48 V/12 V (buck)	ZVS/ZCS 95.2 %@300 W Si-MOSFET (BSC098N10NS5)	370 W/in^3
LLC[30]	isolated	1.2–2.5 MHz /300 kHz	PWM	48 V/12 V (buck)	ZVS 94.5 %@700 W GaN-HEMT	49 W/in^3
Class-E2[31]	nonisolated	20 MHz	ON/OFF	9-18 V/5 V (buck)	ZVS 75 %@10 W GaN-HEMT (EPC2016)	–
Active clamped[32]	isolated	2 MHz	PWM	18 V/5 V (buck)	ZVS 93.5 %@25 W Si-MOSFET (BSC097N06NS)	–
Two-phase buck[33]	nonisolated	1 MHz	PFM	12 V/4 V (buck)	ZVS 97.5 %@24 W GaN-HEMT (EPC2015C)	–
LLC /parallel[34]	isolated	1 MHz	PFM	12 V/5 V (buck)	ZVS 94 %@240 W GaN-HEMT (EPC2020)	53 W/in^3
Flying Capacitor[35]	Nonisolated	1 MHz	PFM	400 V/178 V (buck)	ZVS 94 %@200 W GaN-HEMT (GS66508B)	–
MHz driving snubberless[23]	isolated	1–2 MHz	PFM	10 V/85 V (boost)	ZCS 86.1 %@70 W GaN-HEMT (PGA26E19BA)	17 W/in^3
Proposed converter	isolated	1–2 MHz	PFM	10 V/160 V (boost)	ZCS 91.3 %@104 W GaN-HEMT (GS61004B)	39 W/in^3

*Counted by a discrete power device.

The power loss breakdown relevant to Fig. 17 is revealed in Fig. 18. The conduction losses of active switches and copper losses of HF-X account for a large part of the total loss. The iron loss is less than 1.2% in the total loss, thus is included in the "Other losses." The conduction losses in the secondary side are relatively high as compared to the primary side due to the multiresonant tanks. The power loss in the gate resistor is calculated with the gate charge $Q_g = 3.3\,\mathrm{nC}$, the gate driving voltage $V_{DR} = 6\,\mathrm{V}$ at $f_s = 1.5\,\mathrm{MHz}$ as

$$P_D = Q_g \times V_{DR} \times f_s = 30\,\mathrm{mW} \tag{38}$$

which accounts for about 0.3% in the total power loss.

The thermography image of the prototype in 10 min after the start-up is shown in Fig. 19. The temperatures of Q_1 and Q_2 are measured as 43.2 °C and 35.6 °C, respectively. The dc inductor, parallel resonant inductor, HF-X, and diode rectifiers have temperatures as 25.4 °C, 43.5 °C, 32.7 °C, and 38.6 °C, respectively. It should be remarked here that Q_1 has higher temperature than Q_2 due to the shorter distance from the HF-X.

The comparisons with the existing topologies are summarized in Table III in terms of modulation, voltage conditions, efficiency, and power density. It can be understood hereby that the proposed topology has competitive efficiency and power density as a high step-up MHz-driven dc–dc converter while almost all the existing topologies are limited to buck type which are prone to have higher efficiency due to less conduction losses in active switches.

V. CONCLUSION

A MHz-driving snubberless ZCS high step-up dc–dc converter with multiresonant circuitry has been proposed in this article. The multiresonant tank works for high step-up ratio without loosing the simplicity in the snubberless circuit topology and the low ripple in the input stage of the dc–dc power converter. The frequency-domain analysis has revealed the design guideline of the circuit parameters of the anti and parallel load resonant

TABLE IV
STEADY-STATE EQUATIONS IN EACH MODE FOR THE HALF CYCLE

Intervals	Primary-side L-C network
Mode 1: $t \in [0, t_1]$	$V_{L1} - V_{L2} + aLp\frac{d}{dt}i_{Lp}(t) - Lr\frac{d}{dt}i_{L2}(t) + \frac{aVo}{2} = 0$ $v_{Ca}(t) = L_p\frac{di_{Lp}}{dt}(t) + \frac{V_o}{2} = L_m\frac{di_{Lm}}{dt}$ $C_a\frac{dV_{Ca}}{dt}(t) + i_{Lm}(t) + i_{Lp}(t) = -ai_{L2}(t)$ $V_{L1} = V_{in}$ $V_{L1} = L\frac{d}{dt}i_{L1}(t) - M\frac{d}{dt}i_{L2}(t)$ $V_{L2} = L\frac{d}{dt}i_{L2}(t) - M\frac{d}{dt}i_{L1}(t)$
Mode 2 and 3: $t \in [t_1, t_3]$	$i_{L1}(t) = i_{L1}(t_1) + \frac{Vin(t-t_1)(k+1)}{L(1-k^2)}$ $i_{L2}(t) = i_{L2}(t_1) + \frac{V_{in}(t-t_1)(k+1)}{L(1-k^2)}$ $aL_p\frac{di_{Lp}}{dt}(t) - L_r\left(-\frac{di_{Q2}}{dt}(t) + \frac{Vin(k+1)}{L(1-k^2)}\right) + \frac{aV_o}{2} = 0$ $v_{Ca}(t) = L_p\frac{di_{Lp}}{dt}(t) + \frac{V_o}{2} = L_m\frac{di_{Lm}(t)}{dt}$ $C_a\frac{dv_{Ca}(t)}{dt} + i_{Lm}(t) + i_{Lp}(t) = -a\left(I_{L2}(t_1) + \frac{Vin(t-t_1)(k+1)}{L(1-k^2)}\right) + ai_{Q2}(t)$ $I_{L1}(t_1) + I_{L2}(t_1) + \frac{2V_{in}(t-t_1)(k+1)}{L(1-k^2)} = i_{Q1}(t) + i_{Q2}(t)$
Mode 4: $t \in [t_3, t_4]$	$V_{L1} - V_{L2} + Lr\frac{di_{L1}(t)}{dt} + aV_{Ca}(t) = 0$ $V_{Ca}(t) = L_p\frac{di_{Lp}(t)}{dt} + \frac{1}{Cp}\int_{t_7}^{t} i_{Lp}(\tau)\,dt = L_m\frac{di_{Lm}(t)}{dt}$ $C_a\frac{dV_{Ca}(t)}{dt} + i_{Lm}(t) + i_{Lp}(t) = ai_{L1}(t)$ $V_{L2} = V_{in}$

circuits, then selection guideline of the coupling coefficient of the dc inductors has been theoretically provided by the steady-state characteristics for the input and dc inductor currents. In order to demonstrate the performances of the proposed dc–dc converter, the 1-2 MHz / 120 W prototype has been built, and the snubberless ZCS operations under MHz driving and low ripple rations less than 1% have been verified by experiments as well as steady-state characteristics.

It has also been proven that the EMI noises are well reduced (29%–79%) owing to the soft switching techniques as compared to the hard switching from the spectrums of radiation noises. The dc–dc voltage ratio increases more than 1.5 times as the existing snubberless dc–dc converter, thus high step-up operation has been clarified. The actual efficiency is recorded as 91.3% at 86.5% load while the power dissipation of magnetic components should be reduced for further efficiency improvement under the conditions of MHz driving.

The future researches include enhancement of power rating and power conversion efficiency by optimizing the design of magnetic components suitable for MHz driving. Furthermore, the validity of the closed loop controller will be demonstrated by experiments for steady-state and dynamics operations.

APPENDIX

The steady-state equations of each modes are summarized in Table IV. Note here that the steady-state equations for the other half cycle operations (Mode 5-8) are symmetrical to those in Table IV. The voltage and current waveforms at each mode can be derived by giving the initial values at the mode 1, and solving the high-order equations with the aid of computer calculations.

ACKNOWLEDGMENT

The authors would like to appreciate Mr. Ryusei Miyazaki for the cooperations in analysis and experiments.

REFERENCES

[1] S. Liu, M. Liu, S. Han, X. Zhu, and C. Ma, "Tunable class E2 DC-DC converter with high efficiency and stable output power for 6.78-MHz wireless power transfer," *IEEE Trans. Power Electron.*, vol. 33, no. 8, pp. 6877–6886, Aug. 2018.

[2] N. Weitz, S. Utzelmann, S. Ditze, and M. Marz, "A resonant push-pull DC-DC converter with an intrinsic current source behavior for radio frequency power conversion," *IEEE Trans. Power Electron.*, vol. 37, no. 6, pp. 7001–7012, Jun. 2022.

[3] A. Hariya et al., "Circuit design techniques for reducing the effects of magnetic flux on GaN-HEMTs in 5-MHz 100-W high power-density LLC resonant DC-DC converters," *IEEE Trans. Power Electron.*, vol. 32, no. 8, pp. 5953–5963, Aug. 2017.

[4] Y. Shen, H. Wang, Z. Shen, Y. Yang, and F. Blaabjerg, "A 1-MHz series resonant DC-DC converter with a dual-mode rectifier for PV microinverters," *IEEE Trans. Power Electron.*, vol. 34, no. 7, pp. 6544–6564, Jul. 2019.

[5] M. L. Alghaythi, R. M. OConnell, N. E. Islam, M. M. S. Khan, and J. M. Guerrero, "A high step-up interleaved DC-DC converter with voltage multiplier and coupled inductors for renewable energy systems," *IEEE Access*, vol. 8, pp. 123165–123174, 2020.

[6] K.-C. Tseng, J.-T. Ling, and C.-C. Huang, "High step-up converter with three-winding coupled inductor for fuel cell energy source applications," *IEEE Trans. Power Electron.*, vol. 30, no. 2, pp. 574–581, Feb. 2015.

[7] J.-W. Kim, M.-H. Park, J.-H. Han, M. Lee, and J. S. Lai, "PWM resonant converter with asymmetric modulation for ZVS active voltage doubler rectifier and forced half resonance in PV application," *IEEE Trans. Power Electron.*, vol. 35, no. 1, pp. 508–521, Jan. 2020.

[8] A. Iqbal, S. Gore, P. K. Maroti, S. Islam, M. Meraj, and M. Marzband, "A new triswitching double duty high voltage gain boost converter for DC nanogrid application," *IEEE Trans. Ind. Appl.*, vol. 59, no. 5, pp. 6242–6250, Sep./Oct. 2023.

[9] S. W. Seo, J.-H. Ryu, Y. Kim, and H. H. Choi, "Transformerless quadruple high step-up DC-DC converter using coupled inductors," *IEEE Access*, vol. 10, pp. 26501–26531, Mar. 2022.

[10] V. Marzang, S. M. Hashemzadeh, P. Alavi, A. Khoshkbar-Sadigh, S. H. Hosseini, and M. Z. Malik, "A modified triple-switch triple-mode high step-up DC-DC converter," *IEEE Trans. Ind. Electron.*, vol. 69, no. 8, pp. 8015–8027, Aug. 2022.
[11] X. Pan, H. Lai, Y. Liu, T. Zhao, H. Ju, and A. H. Rathore, "An overview and comprehensive comparative evaluation of current-fed-isolated-bidirectional DC/DC converter," *IEEE Trans. Power Electron.*, vol. 35, no. 3, pp. 2737–2763, Mar. 2020.
[12] H. Moradisizkoohi, N. Elsayad, and O. A. Mohammed, "An integrated interleaved ultrahigh step-up DC-DC converter using dual cross-coupled inductors with built-in input current balancing for electric vehicles," *IEEE J. Emerg. Sel. Topics Power Electron.*, vol. 8, no. 1, pp. 644–657, Mar. 2020.
[13] A. Manuel, S. S. Andrade, L.. Schuch, and M. Martins, "Analysis and design of high-efficiency hybrid high step-up DC-DC converter for distributed PV generation systems," *IEEE Trans. Ind. Electron.*, vol. 66, no. 5, pp. 3860–3868, May 2019.
[14] S. V. Arújo, R. P. Torrico-Bascopé, and G. V. Torrico-Bascopé, "Highly efficient high step-up converter for fuel-cell power processing based on three-state commutation cell," *IEEE Trans. Ind. Electron.*, vol. 57, no. 6, pp. 1978–1988, Jun. 2010.
[15] Y. Hu et al., "Ultrahigh step-up DC-DC converter for distributed generation by three degrees of freedom (3DoF) approach," *IEEE Trans Power Electron.*, vol. 31, no. 7, pp. 4930–4941, Jul. 2016.
[16] C. Nagesha and N. Lakshminarasamma, "High-gain bidirectional LCLC resonant converter with reconfigurable capability," *IEEE Trans. Power Electron.*, vol. 38, no. 2, pp. 871–1886, Feb. 2023.
[17] S. Son, O. A. Montes, A. Junyent-Ferre, and M. Kim, "High step-up resonant DC/DC converter with balanced capacitor voltage for distributed generation systems," *IEEE Trans. Power Electron.*, vol. 34, no. 5, pp. 4375–4387, May 2019.
[18] S. S. Dobakhshari, J. Milimonfared, M. Taheri, and H. Moradis-izkoohi, "A quasi-resonant current-fed converter with minimum switching losses," *IEEE Trans. Power Electron.*, vol. 32, no. 1, pp. 353–362, Jan. 2017.
[19] M. Mousavi, Y. Sangsefidi, and A. Mehrizi-Sani, "A multistage resonant DC-DC converter for step-up applications," *IEEE Trans. Power Electron.*, vol. 36, no. 8, pp. 9251–9262, Aug. 2021.
[20] T.-J. Liang, R.-Y. Chen, and J.-F. Chen, "Current-fed parallel-resonant DC-AC inverter for cold-cathode fluorescent lamps with zero-current switching," *IEEE Trans. Power Electron.*, vol. 23, no. 4, pp. 2206–2210, Jul. 2008.
[21] Y. Guan, Y. Wang, D. Xu, and W. Wang, "A 1 MHz half-bridge resonant DC/DC converter based on GaN FETs and planar magnetics," *IEEE Trans. Power Electron.*, vol. 32, no. 4, pp. 2876–2891, Apr. 2017.
[22] E. Persson, "Optimizing PCB layout for HV GaN power transistors," *IEEE Power Electron. Mag.*, vol. 10, no. 2, pp. 65–78, Jun. 2023.
[23] T. Mishima, R. Miyazaki, and C.-M. Lai, "GaN-HEMT MHz-driving current-fed snubberless ZCS high step-up DC-DC converter for fuel cell vehicles," in *Proc. IEEE Int. Future Energy Electron. Conf.*, Taipei, Taiwan, 2021, pp. 1–6.
[24] T. Mishima and M. Nakaoka, "A practical ZCS-PWM boost DC-DC converter with clamping diode-assisted active edge-resonant cell and its extended topologies," *IEEE Trans. Ind. Electron.*, vol. 60, no. 6, pp. 2225–2236, Jun. 2013.
[25] B. Yuan, X. Yang, D. Li, Y. Pei, J. Duan, and J. Zhai, "A current-fed multiresonant converter with low circulating energy and zero-current-switching for high step-up power conversion," *IEEE Trans. Power Electron.*, vol. 26, no. 6, pp. 1613–1619, Jun. 2011.
[26] R. D. Middlebrook, V. Vorperian, and J. Lindal, "The N extra element theorem," *IEEE Trans. Circuits Syst.–I: Fundam. Theory Appl.*, vol. 45, no. 9, pp. 919–935, Sep. 1998.
[27] Y. Liu, A. Kumar, J. Lu, D. Maksimovic, and K. K. Afridi, "New design methodology for megahertz-frequency resonant DC-DC converters using impedance control network architecture," in *Proc. IEEE Appl. Power Electron. Conf. Expo.*, 2016, pp. 1392–1397.
[28] Z. Saadatizadeh and H. A. Mantooth, "High-frequency fully-ZVS isolated current-fed bidirectional DC-DC converter," in *Proc. IEEE Appl. Power Electron. Conf. Expo.*, 2023, pp. 2213–2217.
[29] T. Liu, Y. Han, X. Wu, S. Yang, and G. Xie, "A MHz regulated DC transformer with wide voltage range," in *Proc. IEEE Int. Power Electron. Appl. Conf. Expo.*, Shenzhen, China, 2018, pp. 1–4.
[30] C. Armbruster, A. Hensel, A. H. Wienhausen, and D. Kranzer, "Application of GaN power transistors in a 2.5 MHz LLC DC/DC converter for compact and efficient power conversion," in *Proc. 18th Eur. Conf. Power Electron. Appl.*, 2016, pp. 1–7.
[31] Y. Li, X. Ruan, L. Zhang, J. Dai, and Q. Jin, "Variable switching frequency ON–OFF control for class E DC-DC converter," *IEEE Trans. Power Electron.*, vol. 34, no. 9, pp. 8859–8870, Sep. 2019.
[32] C. Nan, R. Ayyanar, and Y. Xi, "A 2.2-MHz active-clamp buck converter for automotive applications," *IEEE Trans. Power Electron.*, vol. 33, no. 1, pp. 460–472, Jan. 2018.
[33] Y. Dou, Z. Ouyang, and M. A. E. Andersen, "Integrated coupled inductors with functionality of current balancing transformer for two-phase synchronous DC-DC converters," *IEEE Trans. Power Electron.*, vol. 35, no. 5, pp. 4472–4476, May 2020.
[34] Y.-F. Wang, B. Chen, Y. Hou, Z. Meng, and Y. Yang, "Analysis and design of a 1-MHz bidirectional multi-CLLC resonant DC-DC converter with GaN devices," *IEEE Trans. Ind. Electron.*, vol. 67, no. 2, pp. 425–1434, Feb. 2020.
[35] N. A. Dung, H.-J. Chiu, Y.-C. Liu, and P. J. Huang, "Analysis and implementation of a high voltage gain 1 MHz bidirectional DC-DC converter," *IEEE Trans Ind. Electron.*, vol. 67, no. 2, pp. 1415–1424, Feb. 2020.

Tomokazu Mishima (Senior Member, IEEE) received the Ph.D. degree in electrical engineering from University of Tokushima, Tokushima, Japan, in 2004.

Since 2010, he has been an Associate Professor engaged in the researches and developments of power electronics circuits and systems, with Kobe University, Hyogo, Japan, where he has been appointed to the Center for Advanced Medical Engineering Research and Development (CAMED), in 2020, and the research center for Hydrogen Energy Technology (HyTec), in 2024. His research interests include soft-switching dc–dc converters, resonant converters, and high-frequency inverters for industrial, automotive, biomedical, renewable, and sustainable energy applications.

Dr. Mishima is a Senior Member of The Institute of Electrical Engineering of Japan (IEEJ), and Member of the Institute of Electronics, Information and Communication Engineers and the Japan Institute of Power Electronics. He was the recipient of the Best Paper Award in the 2009 IEEE International Conference on Power Electronics and Drive Systems, Best Paper Presentation Award in 2012 Annual Conference of the IEEE Industrial Electronics Society, IEEE TRANSACTIONS ON POWER ELECTRONICS 2017 Outstanding Reviewer Award in 2018, Japan Nikkei Electronics Power Electronics Award in 2021, 2022 IEEE TRANSACTIONS ON POWER ELECTRONICS Second Place Prize Paper Award. He serves as the Associate Editor for IEEE TRANSACTIONS ON POWER ELECTRONICS since 2018, and the chairperson of the semiconductor power converter sector in *IEEJ Transactions on Industry Applications*, in 2023. He was also the chairperson of the IEEJ Investing Research & Development Committee on High-Frequency Switching Power Converters and Applied Power Supplies in 2019–2023.

Shiqiang Liu (Student Member, IEEE) was born in Henan, China, in 1995. He received the B.S. degree in electrical engineering and automation from the Shandong University of Technology, Zibo, China, in 2017, and the M.S. degree in electrical engineering from the Dalian University of Technology, Dalian, China, in 2020. He is currently working toward the Ph.D degree in electrical engineering with the Faculty of Maritime Sciences, Kobe university, Kobe, Japan.

His research interests include bidirectional dc–dc converters, HEV/EV onboard charger, artificial intelligence applications in power electronics, and renewable power conversion systems.

Ryotaro Taguchi was born in Osaka in 2001. He received the B.S. degree in mechatronics engineering in 2024 from Kobe University where he is currently working toward the M.S. degree with the Graduate School of Maritime Sciences.

His M.S. degree research focuses on multiresonant high-frequency-link dc-dc converters. His research interests includes high frequency inverter, and isolated dc-dc converters and applications.

Ching-Ming Lai (Senior Member, IEEE) received the Ph.D. degree in electrical engineering from National Tsing Hua University, Hsinchu, Taiwan, in 2010.

From 2009 to 2012, he was a Senior Research and Development Engineer with Lite-On Technology Corporation, Taipei, Taiwan. From 2014 to 2019, he was a Faculty Member with the Department of Vehicle Engineering, National Taipei University of Technology, Taipei, Taiwan. Since 2019, he has joined the Department of Electrical Engineering, National Chung Hsing University (NCHU), Taichung, Taiwan, where he is currently the Professor and the Director of the Intelligent Electric Vehicle & Green Energy Center. From February to August 2023, he was a Research Professor with Kobe University, Kobe, Japan. His research interests include electric vehicles, power electronics, green energy technologies, and intelligent transportation.

Dr. Lai is a Fellow of Institution of Engineering and Technology and Fellow of the Australian Institute of Energy. He was the recipient of the 2008 Young Author's Award for Practical Application from the Society of Instrument and Control Engineers, Japan, and the Best Paper Award at the 2013 IEEE International Conference on Power Electronics and Drive Systems, and several distinguished awards, including the Dr. Shechtman Youth Researcher Award from Taipei Tech in 2018, the Outstanding Youth Electrical Engineer Award from the Chinese Institute of Electrical Engineering in 2018, the Outstanding Education Achievement Award from SAE-Taipei in 2019, the Outstanding Youth Control Engineer Award from the Chinese Automatic Control Society in 2019, the Outstanding Youth Engineer Award from the Chinese Institute of Engineers-Taichung Chapter in 2020, the NCHU Outstanding Industry-Academia Collaboration Award from 2021–2023, and the Ta-You Wu Memorial Award from National Science and Technology, Taiwan, in 2023. In addition, according to Elsevier, he was listed in the World's Top two of Scientists (Field: Energy) by field in 2021, 2022, and 2023. He was the Co-Chair of IEEE International Future Energy Electronics Conference (IFEEC)-2021, the Tutorial Chair of IEEE IFEEC-2021, IEEE Annual Workshop on Wide Bandgap Power Devices and Applications-2019, and IEEE IFEEC-2015. He has been serving as an Editor for the IEEE TRANSACTIONS ON VEHICULAR TECHNOLOGY since 2017, and an Associate Editor for IEEE ACCESS since 2021.